Electronic Supplementary Material (ESI) for ChemComm.

Supporting Information

Facet-Specific Ligand Dynamics: Scaling the Descriptors of $Cs_2AgBiBr_6$ Nanocrystals

Anamika Mondal,[1] Manuj Ahuja,[2] Priya Johari,[2,*] Sayan Bhattacharyya[1,*]

[1]*Department of Chemical Sciences and Centre for Advanced Functional Materials, Indian Institute of Science Education and Research (IISER) Kolkata, Mohanpur - 741246, India*
[2]*Department of Physics, School of Natural Sciences, Shiv Nadar Institution of Eminence, Greater Noida, Gautam Buddha Nagar, UP 201314, India*

*Email for correspondence: sayanb@iiserkol.ac.in, priya.johari@snu.edu.in

Experimental Section

Chemicals and Materials

$BiBr_3$ (bismuth bromide, 98%, Sigma-Aldrich), $AgNO_3$ (silver nitrate, 99%, Sigma-Aldrich), Cs_2CO_3 (cesium carbonate, 99.995% Sigma-Aldrich), octadecene (ODE, 90% Sigma-Aldrich), oleic acid (OA, 90% Sigma-Aldrich), oleylamine (OLAM, 98%), hexadecylamine (HDA, 90% Sigma-Aldrich), tetradecylamine (TDA, 95% Sigma-Aldrich), dodecylamine (DA, 98% SRL), and HBr (hydrobromic acid, 48-49% in water), were used without further purification.

Synthesis of Cs-oleate

163 mg Cs_2CO_3, 8 ml ODE, and 0.5 ml OA were taken in a 100 mL 3-neck flask, dried, and vacuumed at 100°C for 1 h, and then the temperature of the mixture was raised to 120°C under N_2 atmosphere until the white-colored clear solution of Cs-oleate was obtained.

Synthesis of CABB-OLAM NCs

45 mg $BiBr_3$, 17 mg $AgNO_3$, 4 ml ODE, 1 ml OA, 100 µl HBr, and 1 ml OLAM were mixed in a 25 ml 3-necked round bottom flask and heated to 160°C for 1 h under vacuum to remove residual water and dissolved oxygen. The reaction temperature was increased to 200°C under N_2 atmosphere, and 0.8 ml Cs-oleate stock solution was swiftly injected under stirring. When the precursor salts were dissolved in ODE, the color of the solution was changed to white, then at 160°C, it changed to light yellow, while after Cs-oleate injection at 200°C, the color changed to deep yellow. After 5 sec, the reaction mixture was cooled to room temperature by taking the flask into an ice bath. After centrifugation at 7000 rpm for 10 min, the crude NCs were separated from the solution, further redispersed in chloroform, and centrifuged for 5 min at 10000 rpm, besides discarding the precipitate. The above solution was taken for further NC separation by adding 2 ml of absolute ethanol into the 4 ml above-dispersed chloroform solution and shaking for 30 sec. Afterward, the precipitate was separated by 5 min centrifugation at 12000 rpm. Here 100 µl HBr was mixed with 6 mL solution to ionise the $AgNO_3$ and to remove any AgBr impurity. 200°C is the optimized injection temperature depending on the boiling point of OLAM (348 - 350°C).

Synthesis of CABB-HDA, CABB-TDA, and CABB-DA NCs

The CABB-HDA, CABB-TDA, and CABB-DA NCs were synthesized by a similar procedure except using 0.78 mL HDA (3.03 mmol), 0.65 mL TDA (3.03 mmol) and 0.697 mL DA (3.03 mmol) as the amine ligand, respectively. The optimized HBr amounts for HDA, TDA, and DA were 73, 70, and 67 µL, respectively. 200°C is the injection temperature lower than the boiling point of HDA (322.5°C), TDA (291.2°C), and DA (259°C).

Characterization

XRD measurement was carried out by Rigaku Cu Kα (1.54 Å powder X-ray diffractometer with Cu Kα (λ = 1.54 Å). XRD patterns were refined by Rietveld refinement using GSAS-II software. The 3D views of the crystal structures were obtained by VESTA software. The TEM imaging, FFT patterns, and high-angle annular dark-field – scanning TEM (HAADF-STEM) mapping were obtained from the JEOL JEM-2100F instrument with an operating voltage of

200 kV. TEM analysis was performed by dispersing the as-synthesised NCs in toluene, maintaining a concentration of 0.1µg/µl in all cases. XPS measurements were carried out by mounting the NC samples as pellets on carbon tape in PHI 5000 Versa Probe III at CRF IIT (ISM). Ar^+ ion beam was used as the excitation source. To evaluate the valence states, Fityk software was used to fit the acquired spectra with the Voigt peaks having 20% Lorentzian and 80% Gaussian components. All the XPS data were corrected with respect to the C *1s* spectra. Jasco V-670 spectrophotometer was used to record the optical absorption spectra. Room temperature PL spectra were measured by an FLS 1000 instrument, and the low-temperature PL experiments were performed by the cryostat attachment with liquid N_2 from 80 to 300 K. The excitation source for the PL experiment is an Xe-400 lamp, and the detector is PMT-90A wavelength of 365 nm was used as the excitation wavelength. The samples for PL experiments were prepared by drop-casting on the quartz substrate. Infrared spectral data were collected with a PerkinElmer spectrometer with KBr pellets. To estimate the energy levels of CABB NCs, cyclic voltammograms were recorded in anhydrous acetonitrile solution with tetrabutylammonium hexafluorophosphate ($TBAPF_6$) as a supportive electrolyte at a scan rate of 100 mV/s under N_2 atmosphere at room temperature. A glassy carbon electrode was used as a working electrode, a non-aqueous $Ag/AgNO_3$ electrode was used for the reference electrode, and a Pt wire was used for the counter electrode. The reference was calibrated against the ferrocene/ferrocenium couple. The potential range was between 1.2 V to -1.5 V. The KPFM data was recorded with Cypher ES environmental SPM system, CYPHER-ES-HV. CPD was estimated according to equation (4):

$$CPD = \frac{(\Phi\, Tip - \Phi sample)}{e} \qquad (4)$$

where Φ_{tip} is the tip energy of the platinum tip (5 eV), and Φ_{sample} is the work function of the sample.

Electron-only device fabrication

The electron-only devices were fabricated by spin coating the CABB NC solution on top of the c-TiO_2 coated FTO substrate. 100 mg/ml NC solution was prepared in dry toluene followed by spin coating 70 µL of the above solution on the top of the TiO_2 layer at 2000 rpm for 30 sec. To remove the excess ligands, a mixture of ethanol and 1-octadecene was used to dip the coated films. A ~100 nm thick Au layer was deposited on the top of the CABB NC layer by thermal evaporation.

Computational Studies

All the calculations were performed using the first-principles density functional theory (DFT) implemented in the Vienna *ab initio* simulation package (VASP).[S1] The project augmented-wave (PAW) pseudopotentials were used to treat the electron-ion interactions.[S2] At the same time, the electronic exchange-correlation effects were described using the generalized gradient approximation (GGA) in Perdew-Burke-Ernzerhof (PBE) flavor.[S3] The van der Waals correlations were also incorporated using the DFT-D3 method of Grimme to account for the weak interactions between the ligands and the adsorbent.[S4] All the systems were relaxed using a plane-wave cut-off energy of 520 eV and a *k*-point mesh of 4×4×1. For all the calculations, the convergence criteria for the energy and the Hellmann-Feynman force were set as 10^{-4} eV and 0.01 eV $Å^{-1}$, respectively. At first, the cubic structure of CABB was relaxed, followed by

introducing asymmetrical slabs having two repetition units of the cleaved surface and one asymmetrical layer along the *z*-direction exhibiting the desired (*hkl*) facets on the slab surface. These structures were created from the optimized bulk structure using the pymatgen library and relaxed.[S5] A periodicity was maintained along the *x* and *y*-directions to mimic the surface geometry. At the same time, a vacuum of ~15 Å (post addition of the amine molecule) was introduced along the *z*-direction in all cases.

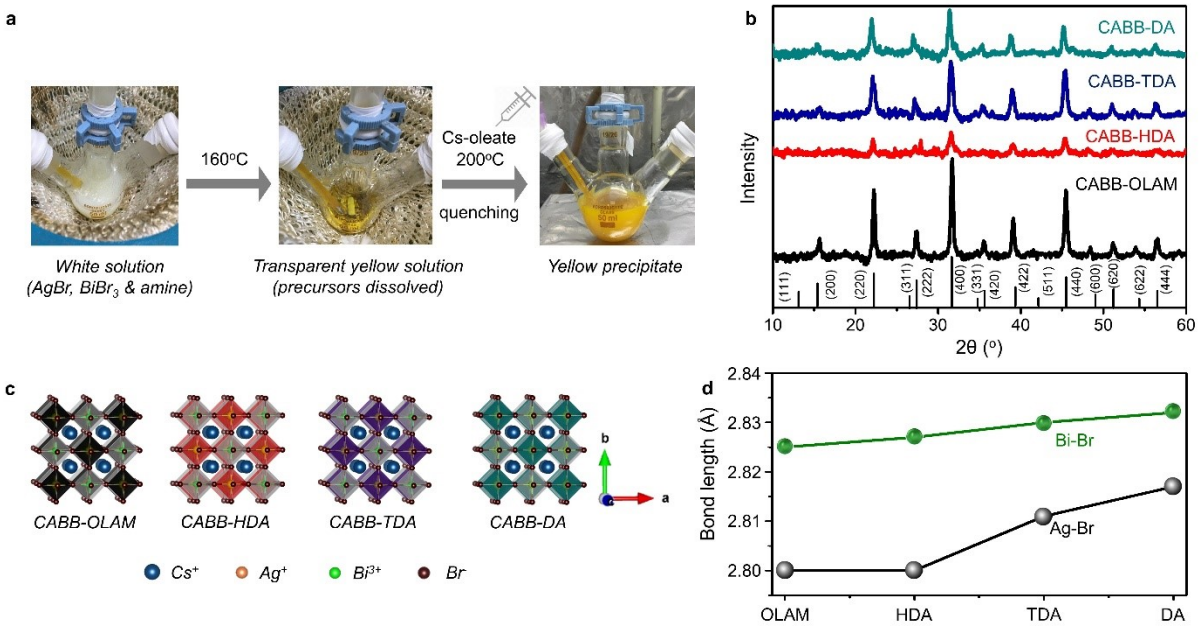

Figure S1. (a) Schematic of the synthesis steps for the preparation of CABB NCs. (b) XRD patterns of CABB-OLAM, CABB-HDA, CABB-TDA and CABB-DA NCs, where the abbreviations are CABB – $Cs_2AgBiBr_6$, OLAM – oleylamine, HDA – hexadecylamine, TDA – tetradecylamine and DA – dodecylamine. (c) The crystal structures obtained from Rietveld refined XRD patterns. (d) Amine chain length dependent variation of Ag-Br and Bi-Br bond lengths.

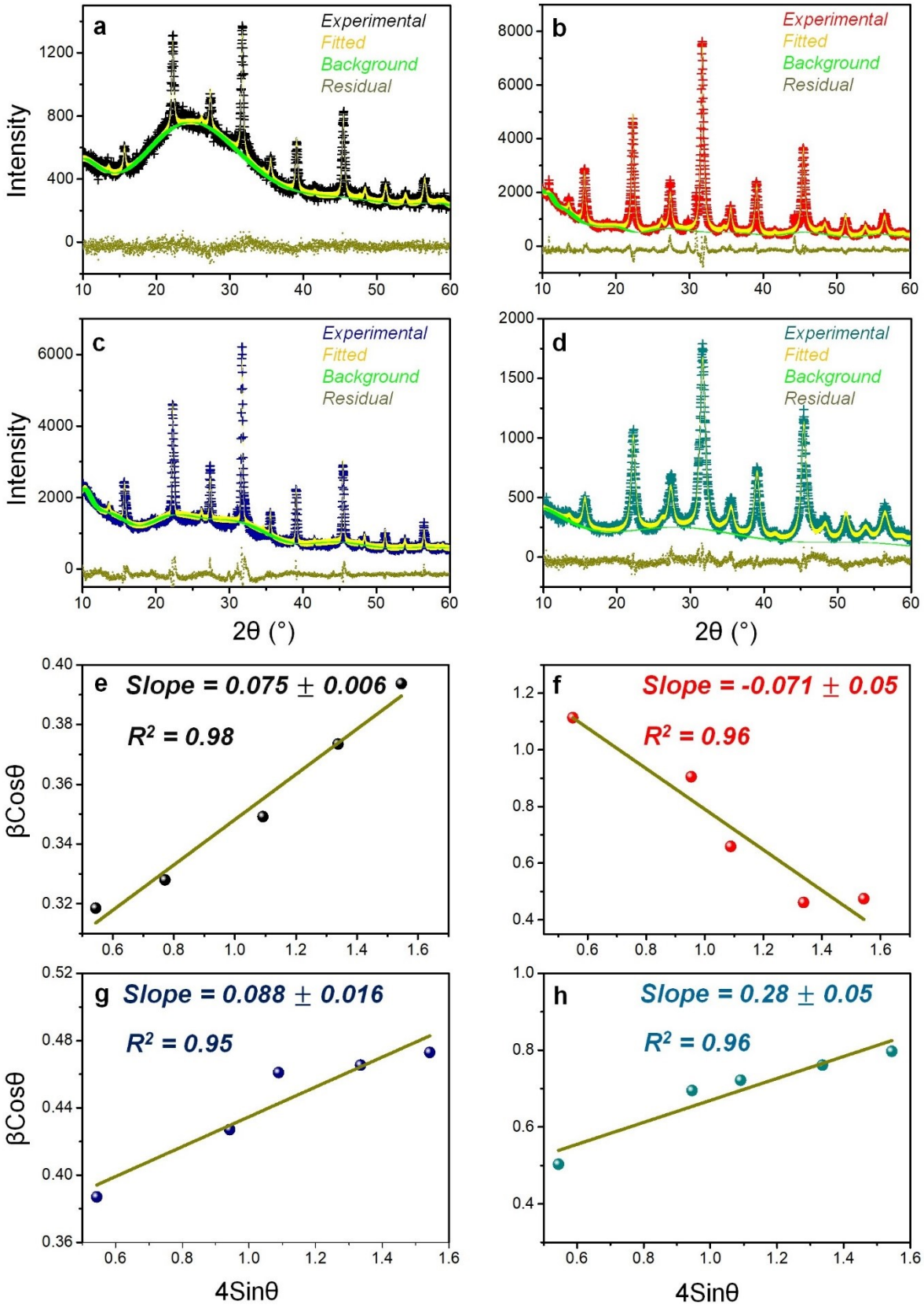
a
Experimental
Fitted
Background
Residual
Intensity
b
c
d
2θ (°)
e Slope = 0.075 ± 0.006
R² = 0.98
f Slope = -0.071 ± 0.05
R² = 0.96
g Slope = 0.088 ± 0.016
R² = 0.95
h Slope = 0.28 ± 0.05
R² = 0.96
βCosθ
4Sinθ

Figure S2. Rietveld refined XRD patterns of (a) CABB-OLAM, (b) CABB-HDA, (c) CABB-TDA and (d) CABB-DA NCs. W-H plots for the calculation of lattice strain of (e) CABB-OLAM, (f) CABB-HDA, (g) CABB-TDA and (h) CABB-DA NCs.

Table S1. Rietveld refined XRD parameters of $Cs_2AgBiBr_6$ NCs of space group $Fm\bar{3}m$: CABB-OLAM, CABB-HDA, CABB-TDA and CABB-DA.

Perovskite	Lattice volume ($Å^3$)	Lattice parameter ($a = b = c$) (Å)	Bond angle ($\alpha = \beta = \gamma$) (°)	GOF	R_{wp} (%)
CABB-OLAM	1434.1	11.27	90	1.03	4.7
CABB-HDA	1434.0	11.27	90	2.3	7.9
CABB-TDA	1439.0	11.29	90	2.3	7.1
CABB-DA	1440.5	11.30	90	1.4	8.1

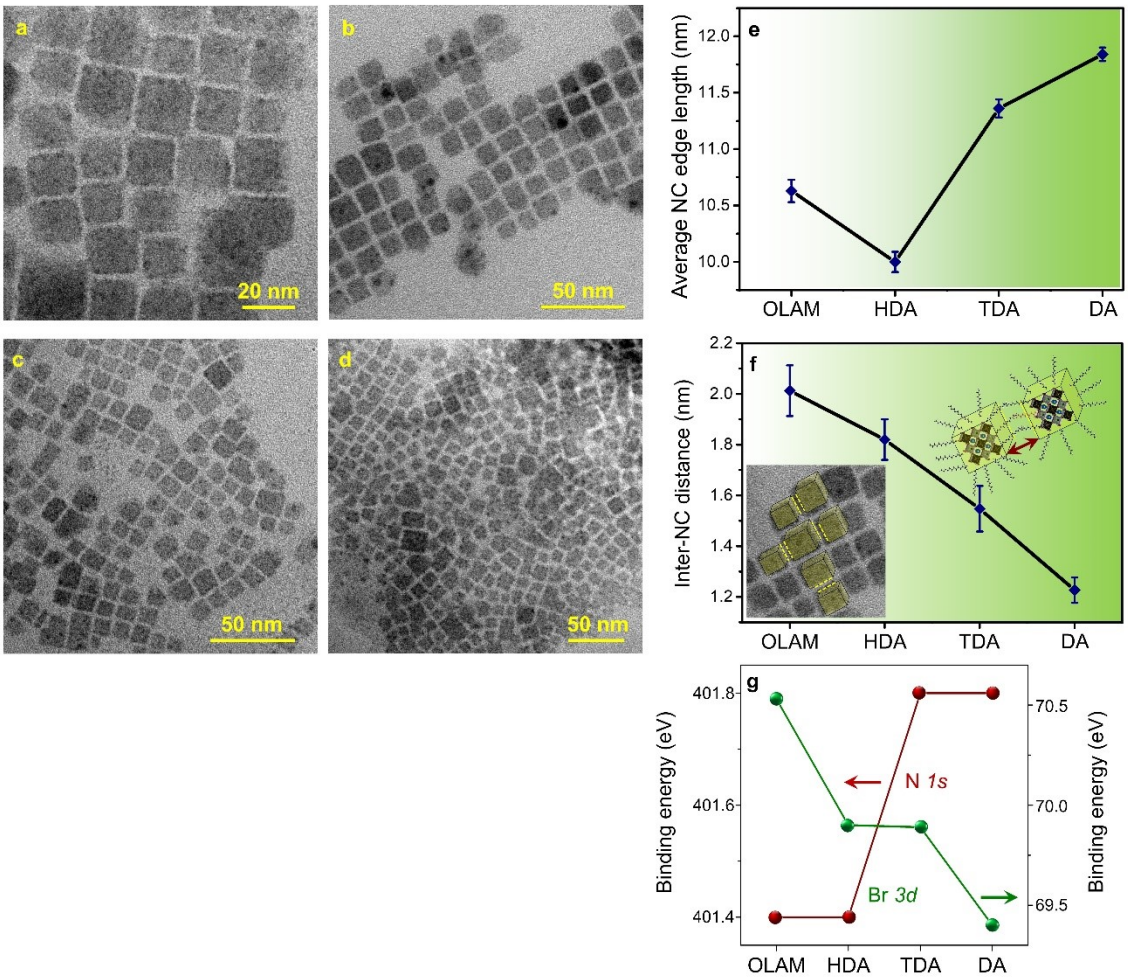

Figure S3. TEM images of (a) CABB-OLAM, (b) CABB-HDA, (c) CABB-TDA, and (d) CABB-DA NCs. (e) Amine chain length dependent variation of the average NC edge length. (f) Amine chain length dependent variation of the inter-NC distance. Insets show the schematic representation of the inter-NC distance (right) and the cartoon overlapping the TEM image for

better visualization (left). (g) Amine chain length-dependent variation of the XPS binding energies of Br *3d*, and N *1s* levels.

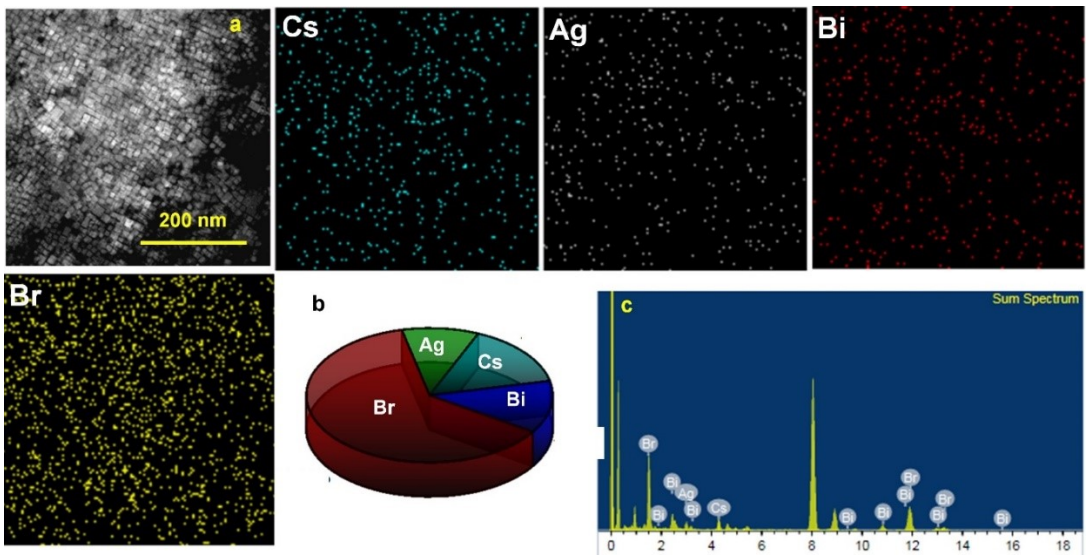

Figure S4. (a) HAADF-STEM image of CABB-DA NCs and the corresponding elemental maps of Cs, Ag, Bi and Br. (b) Pie chart from the (c) EDAX spectrum.

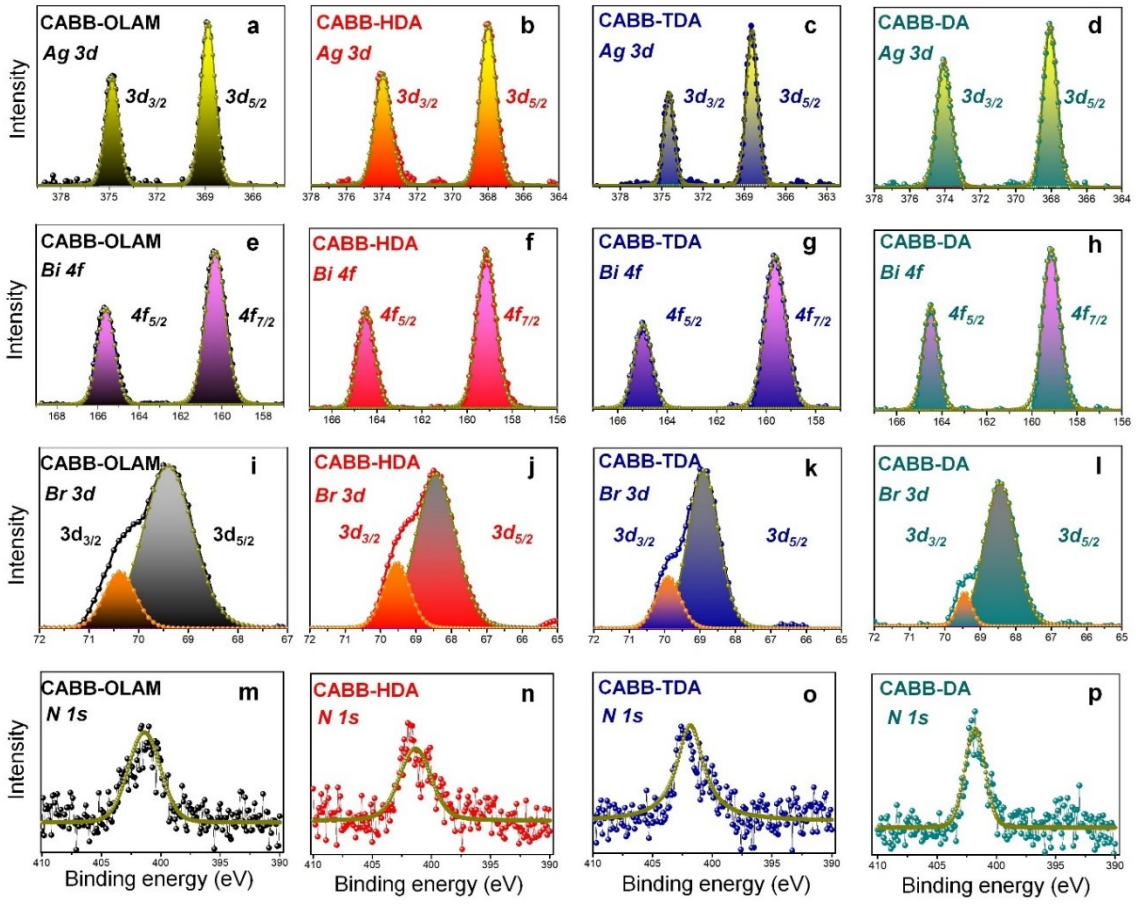

Figure S5. XPS core level spectra of Ag *3d* levels of (a) CABB-OLAM, (b) CABB-HDA, (c) CABB-TDA and (d) CABB DA NCs. XPS core level spectra of Bi *4f* levels of (e) CABB-OLAM, (f) CABB-HDA, (g) CABB-TDA and (h) CABB DA NCs. XPS core level spectra of

Br *3d* levels of (i) CABB-OLAM, (j) CABB-HDA, (k) CABB-TDA and (l) CABB DA NCs. XPS core level spectra of N *1s* levels of (m) CABB-OLAM, (n) CABB-HDA, (o) CABB-TDA and (p) CABB DA NCs.

Table S2. Fitted XPS binding energies for Ag^{+}, Bi^{3+}, Br^{-} and N (NH_3^{+}) species of CABB-OLAM, CABB-HDA, CABB-TDA, CABB-DA.

Core level	Ag $3d_{3/2}$	Ag $3d_{5/2}$	Bi $4f_{5/2}$	Bi $4f_{7/2}$	Br $3d_{3/2}$	Br $3d_{5/2}$	N *1s*
Species	Ag^{+}	Ag^{+}	Bi^{3+}	Bi^{3+}	Br^{-}	Br^{-}	NH_3^{+}
Perovskite	Binding energy (eV)						
CABB-OLAM	374.8	368.8	165.6	160.3	70.5	69.4	401.4
CABB-HDA	374.5	368.4	164.9	159.6	69.9	69.4	401.4
CABB-TDA	374.0	368.0	164.5	159.1	69.9	68.9	401.8
CABB-DA	374.0	368.1	164.5	159.1	69.4	68.4	401.8

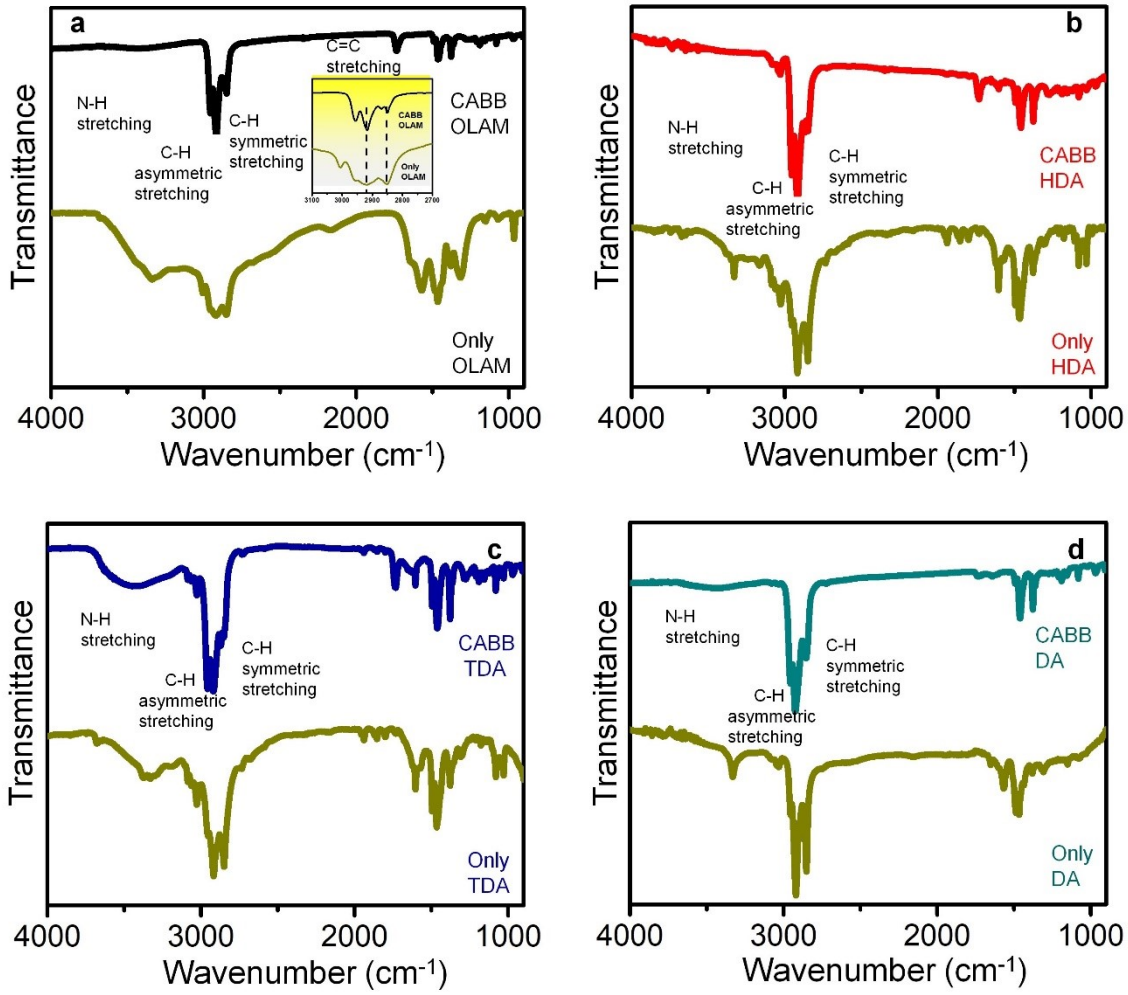

Figure S6. Infrared spectra of (a) CABB-OLAM NCs and only OLAM ligand, (b) CABB-HDA NCs and only HAD ligand, (c) CABB-TDA NCs and only TDA ligand, and (d) CABB DA NCs and only DA ligand. Inset (a) shows the zoom in view of the comparative spectra.

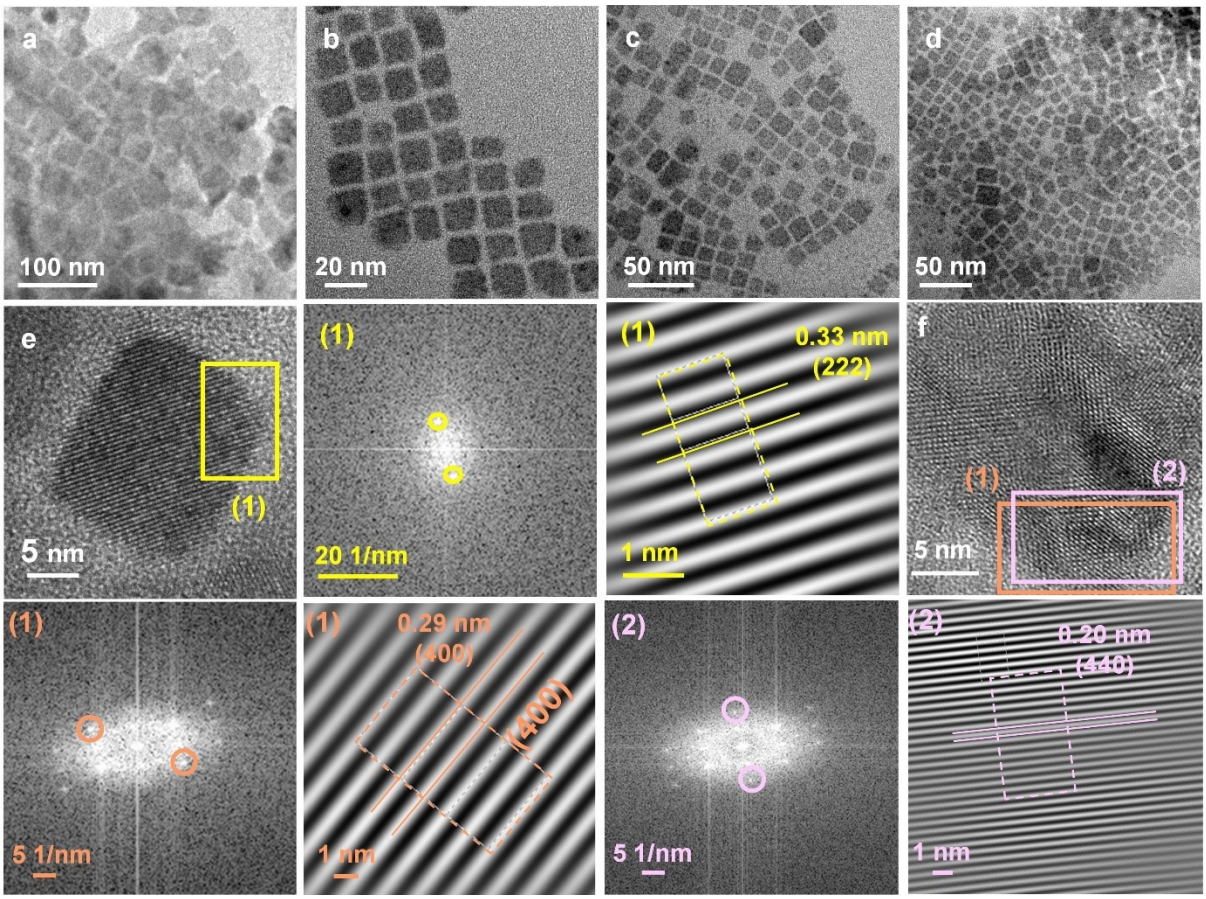

Figure S7. Additional TEM images of (a) CABB-OLAM, (b) CABB-HDA, (c) CABB-TDA and (d) CABB-DA NCs. FFT patterns and the mask-filtered TEM images showing different facets of (e) CABB-OLAM NC (region 1), and (f) CABB-DA NC (regions 1 and 2).

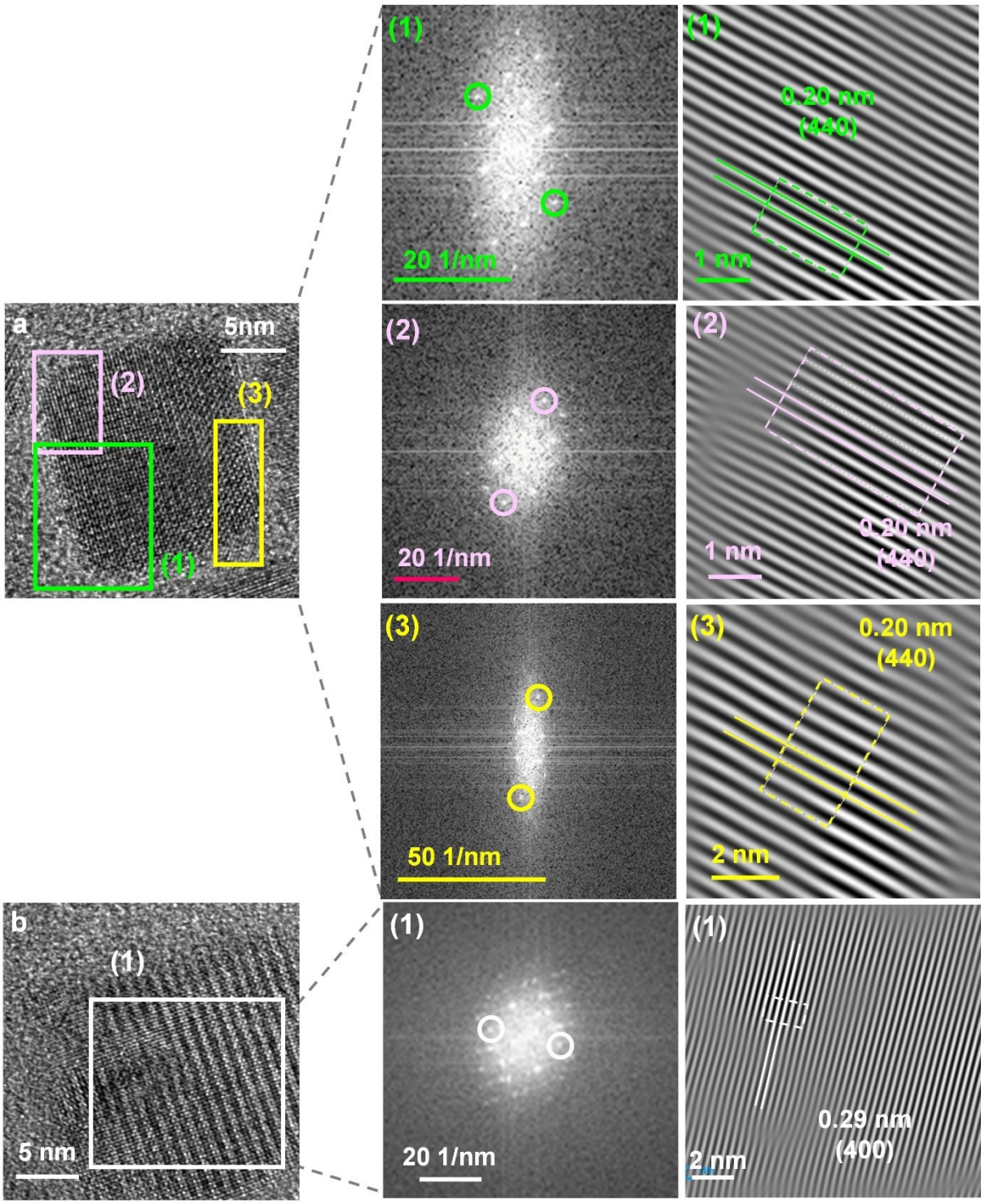

Figure S8. Additional TEM analyses showing different facets of (e) CABB-TDA NC (from regions 1-3), and (b) CABB-DA NC (from region 1).

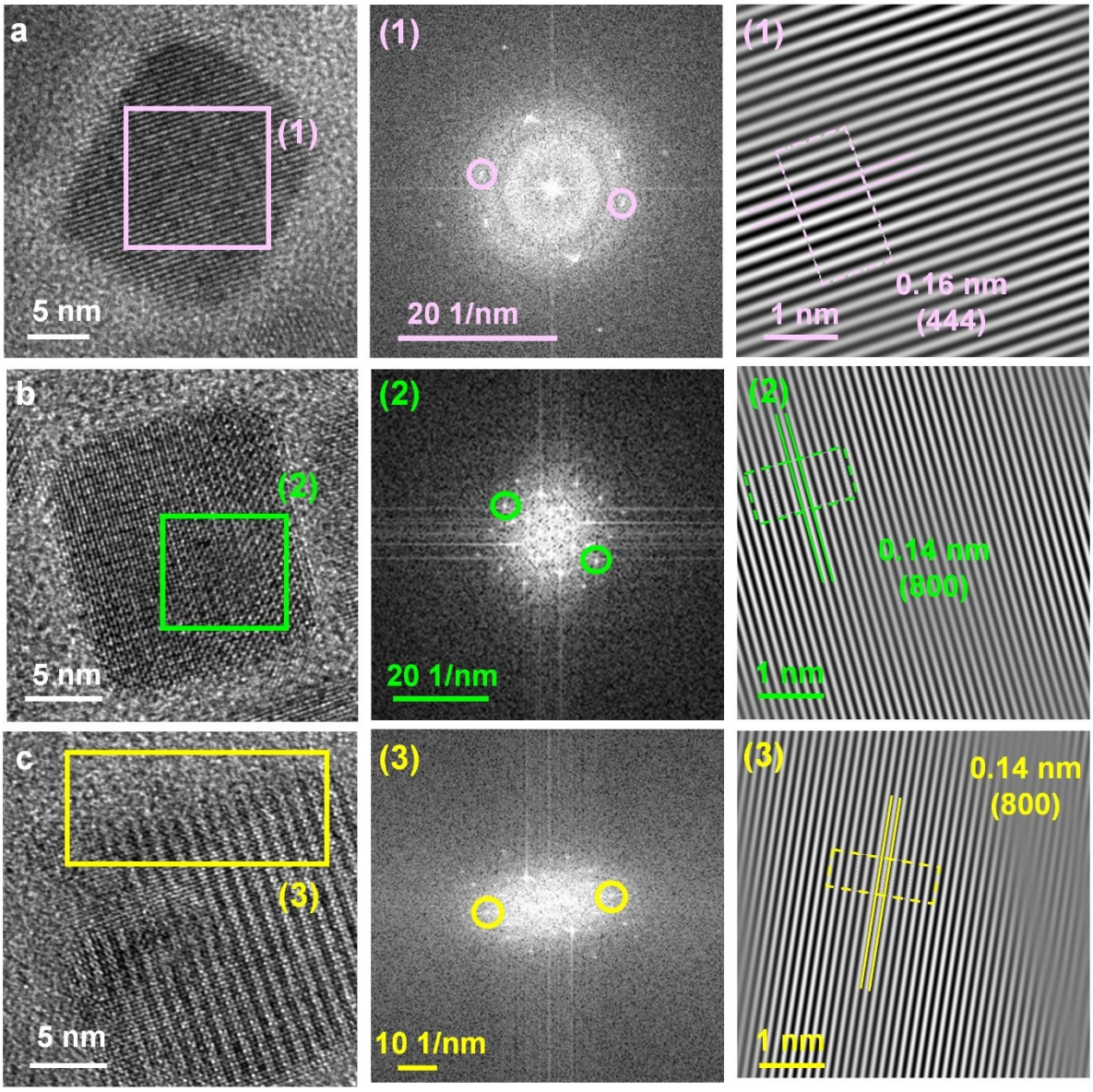

Figure S9. Additional TEM analyses showing different facets of (a) CABB-OLAM NC (from region 1), (b) CABB-TDA NC (from region 2), and (c) CABB-DA NC (from region 3).

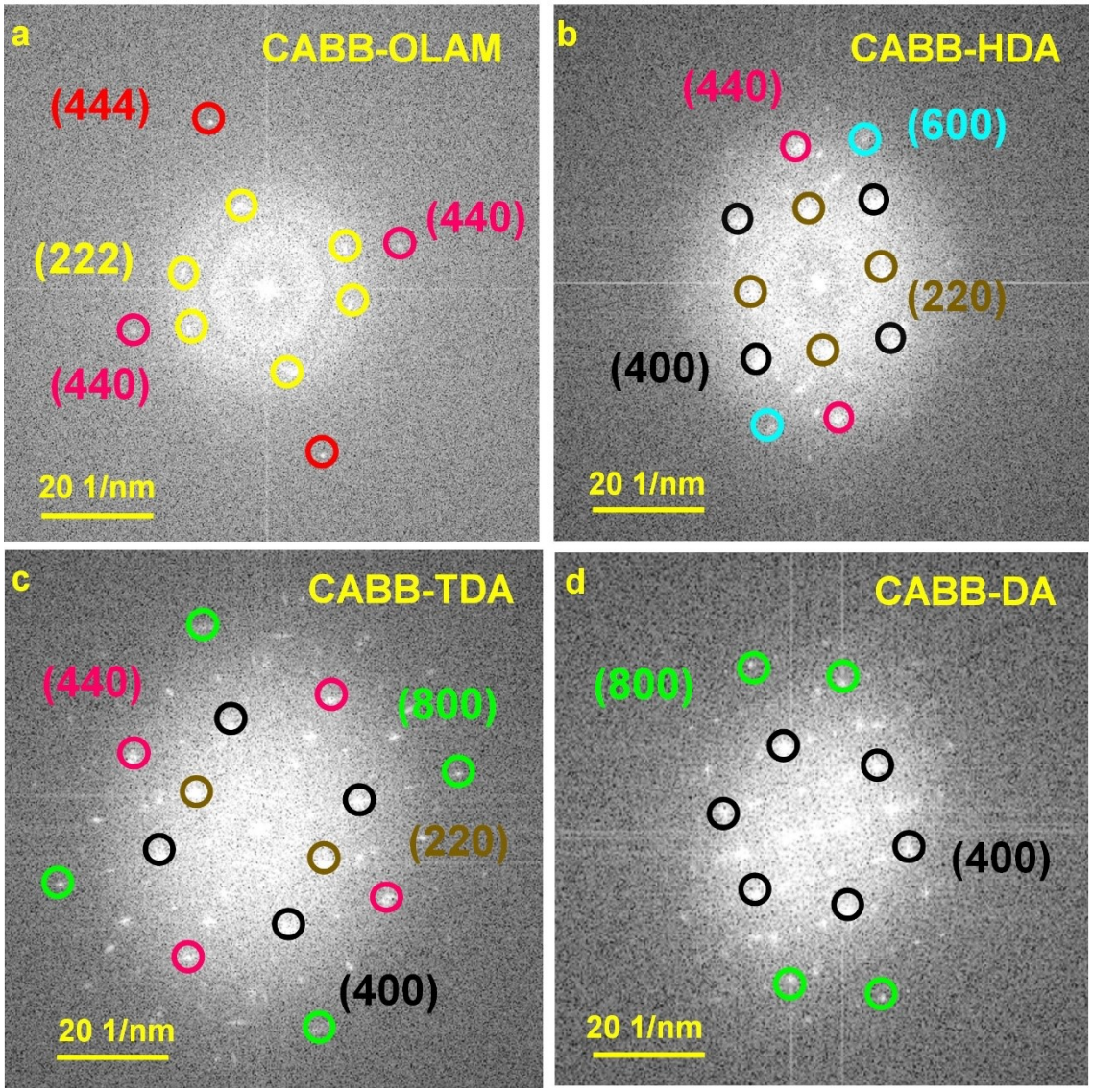

Figure S10. FFT patterns showing the crystallographic facets of (a) CABB-OLAM, (b) CABB-HDA, (c) CABB-TDA, and (d) CABB-DA NCs.

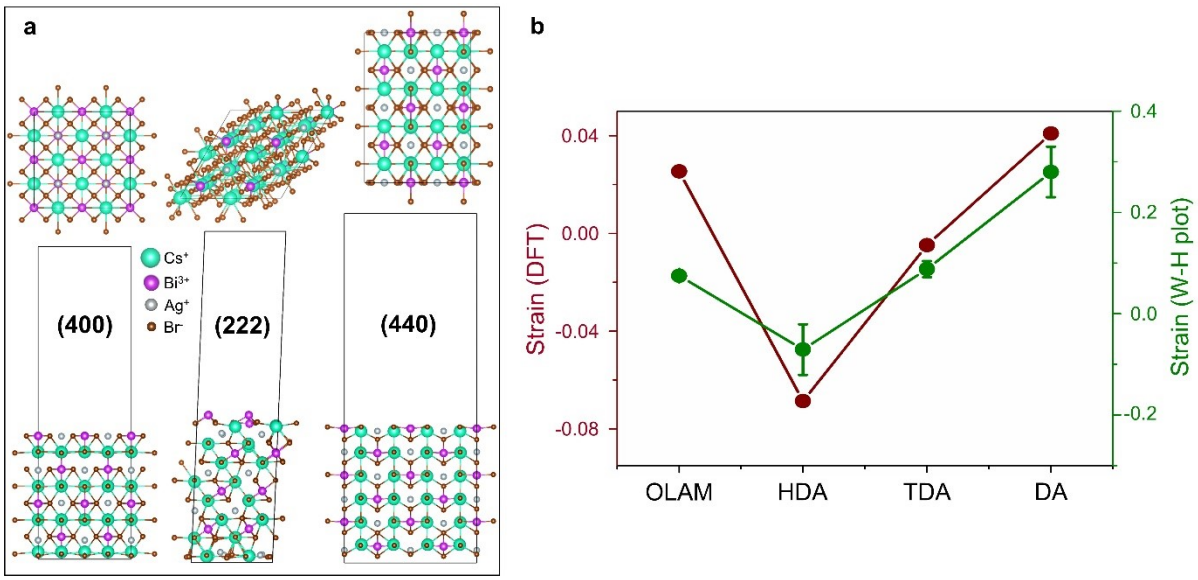

Figure S11. (a) Side and top-views of the optimized geometries of desired (400), (222), and (440) facets on the CABB NC slab surface. (b) Amine chain length-dependent variation of the out-of-plane strain, obtained from DFT analyses, and the experimentally derived lattice strain from W-H plot.

The out-of-plane strain increases from CABB-HDA to CABB-DA NCs, with the former having a negative strain. Instead of decreasing, the strain increases to a positive value in CABB-OLAM NCs, possibly due to a decrease in the effective length of the OLAM (due to curling up). The identical structural variations suggest a similarity between the ligands' measured and computed adsorption sites on the different facets.

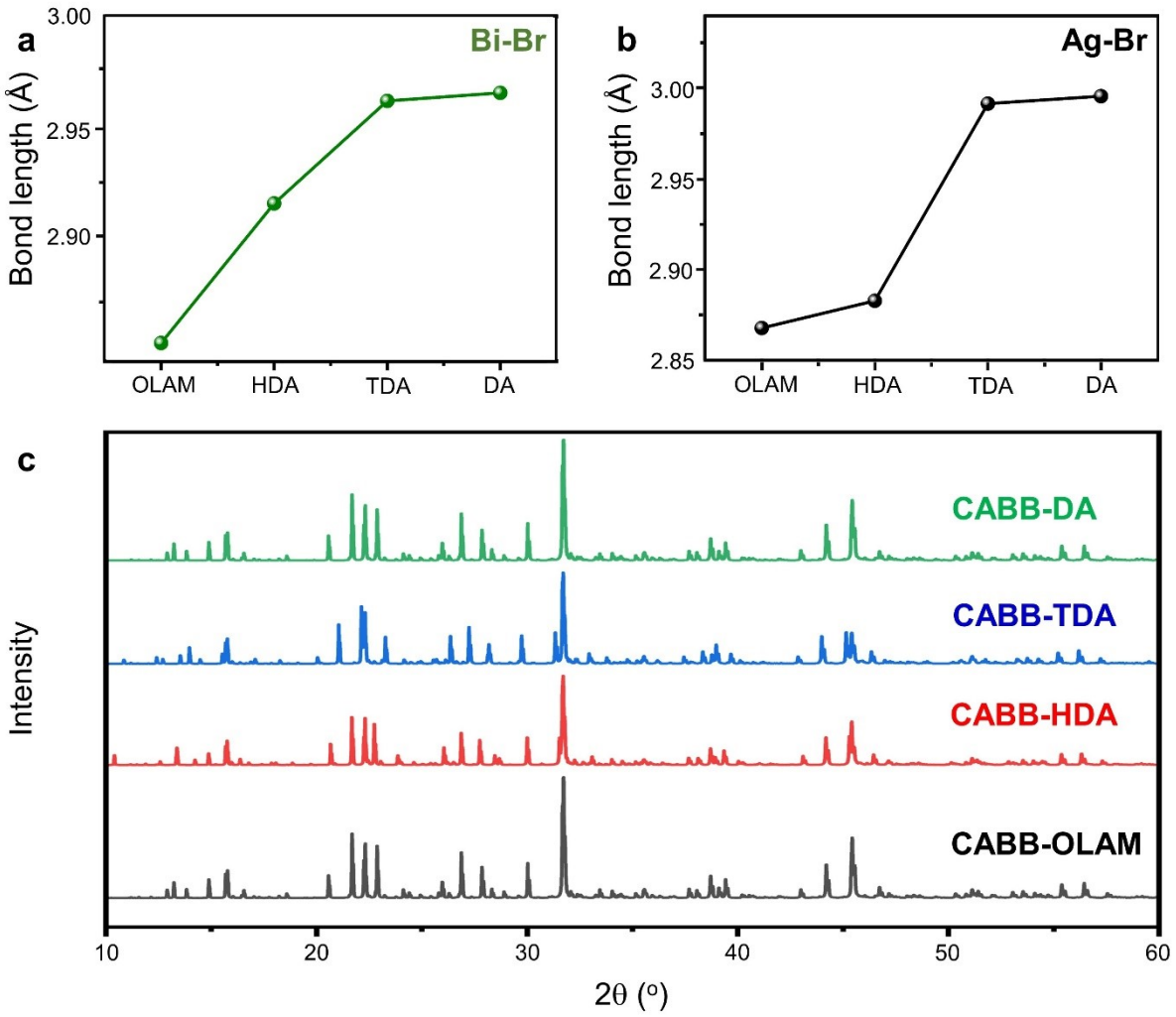

Figure S12. DFT analysed comparison of the (a) Bi-Br, and (b) Ag-Br bond lengths. (c) XRD patterns from the optimized geometry, using VESTA.

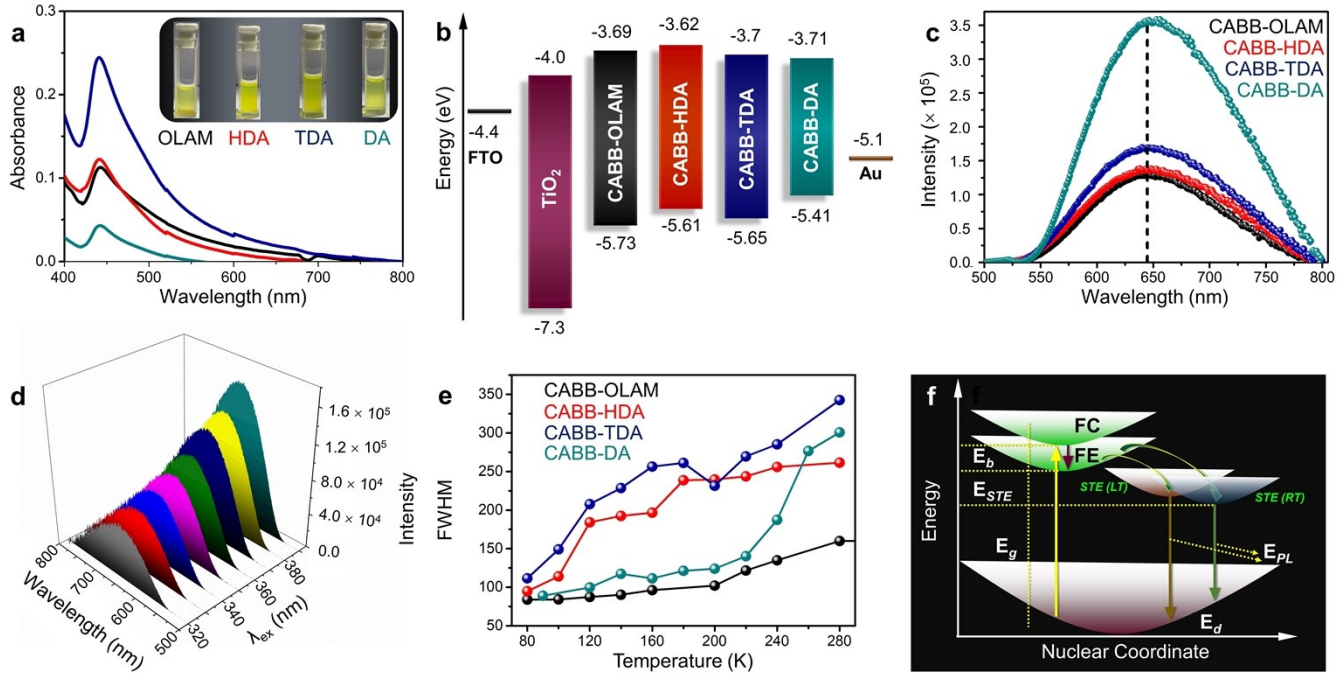

Figure S13. Optical and electronic properties. (a) Optical absorption spectra, (b) energy band diagrams, and (c) PL spectra of CABB-OLAM, CABB-HDA, CABB-TDA and CABB-DA NCs. The inset of panel-a shows the digital images of the NC colloidal solutions. The energy bands were obtained by a combination of the Tauc plot and cyclic voltammetry. (d) Emission map of CABB-DA NCs with respect to different λ_{ex}. (e) Variation of FWHM of the PL bands as a function of temperature for CABB-OLAM, CABB-HDA, CABB-TDA, and CABB-DA NCs. (f) Schematic of the energy level diagram demonstrating the STE emission of the ligand-modified CABB NCs. FC – free charge carrier state, FE – free exciton state, STE (LT) – self-trapped exciton state at lower temperatures, STE (RT) – self-trapped exciton state at room temperature, E_g – band gap energy, E_b - exciton binding energy, E_{STE} - self-trapping energy, E_d - lattice deformation energy, and E_{PL} - emission energy.

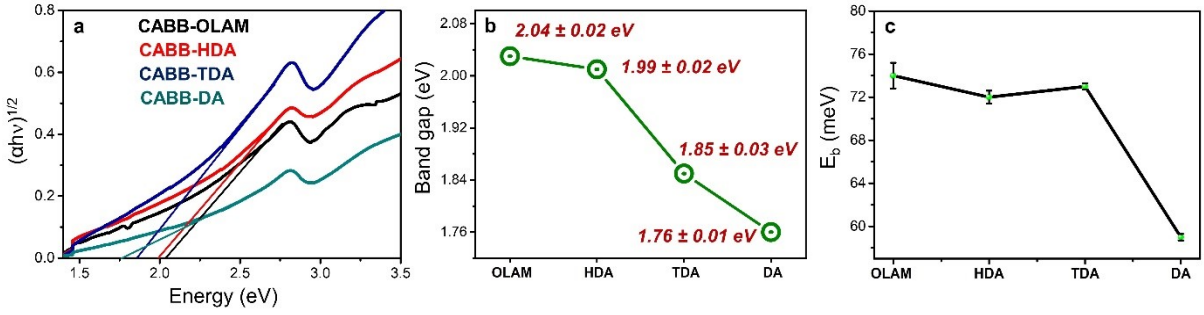

Figure S14. (a) Tauc plots, and the variation of (b) band gap, and (c) exciton binding energy (E_b) for CABB-OLAM, CABB-HDA, CABB-TDA, and CABB-DA NCs.

E_b is estimated experimentally from the temperature-dependent PL spectra by using the Arrhenius equation according to equation (S1):

$$A(T) = A(0)(1 + e^{[-\frac{E_b}{KT}]}) \qquad \text{(S1)}$$

where *A(T)* is the normalized integrated area of the PL band at *T (K)*, *A(0)* is the normalized integrated area at 80 K, and *K* is the Boltzmann constant.

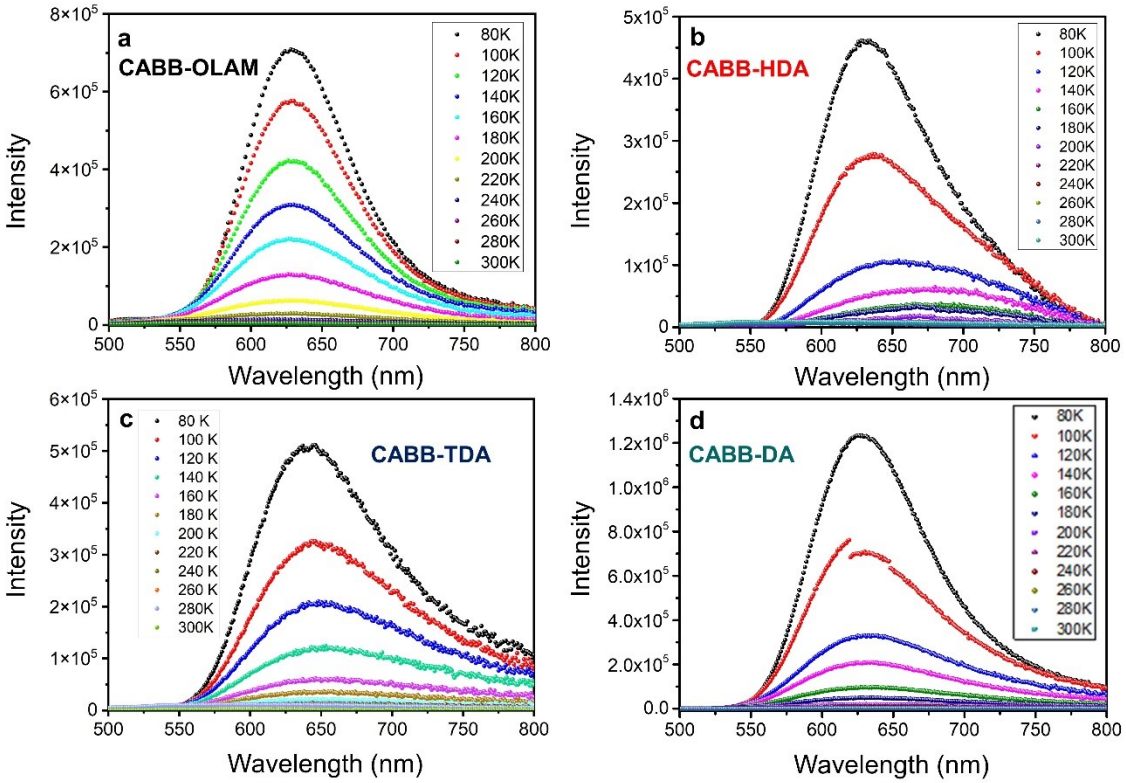

Figure S15. Variable temperature PL spectra of (a) CABB-OLAM, (b) CABB-HDA, (c) CABB-TDA, and (d) CABB-DA NCs.

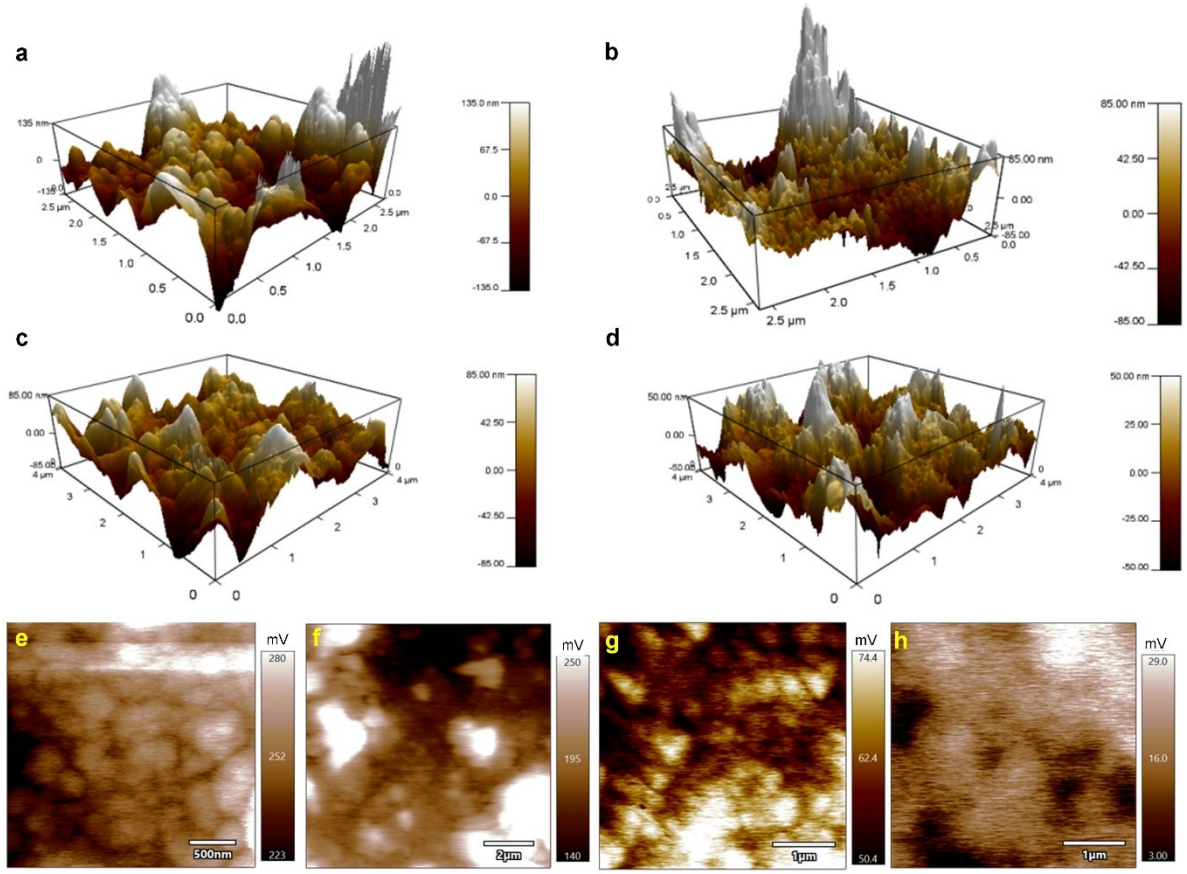

Figure S16. 3D AFM topography on the FTO/c-TiO_2/CABB films showing the 3D height profiles of (a) CABB-OLAM, (b) CABB-HDA, (c) CABB-TDA and (d) CABB-DA NCs. KPFM micrographs showing the CPD profile of (e) CABB-OLAM, (f) CABB-HDA, (g) CABB-TDA, and (h) CABB-DA NCs.

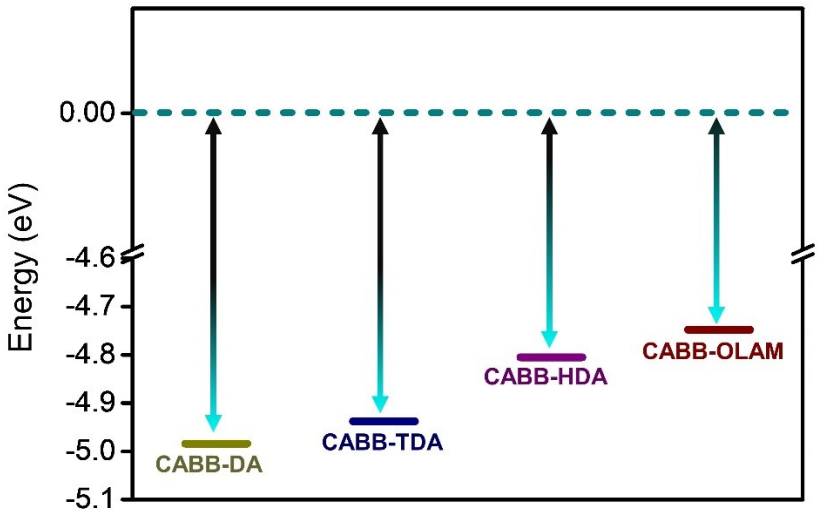

Figure S17. Work function of CABB-OLAM, CABB-HDA, CABB-TDA and CABB-DA NCs, with respect to the vacuum level, estimated from the KPFM measurements. The work function values are 4.75 ± 0.03, 4.81 ± 0.04, 4.94 ± 0.01 and 4.98 ± 0.01 eV for CABB-OLAM, CABB-HDA, CABB-TDA and CABB-DA NCs, respectively.

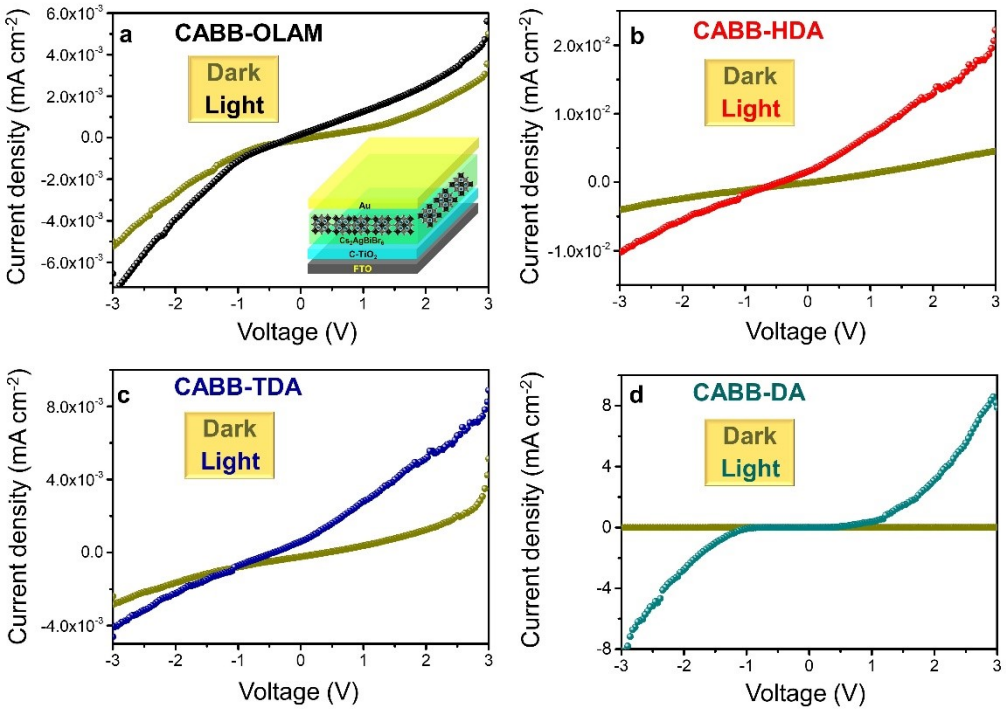

Figure S18. Current-voltage plots under light and dark conditions for (a) CABB-OLAM, (b) CABB-HDA, (c) CABB-TDA, and (d) CABB-DA NCs. Inset of panel-a shows the electron-only device architecture.

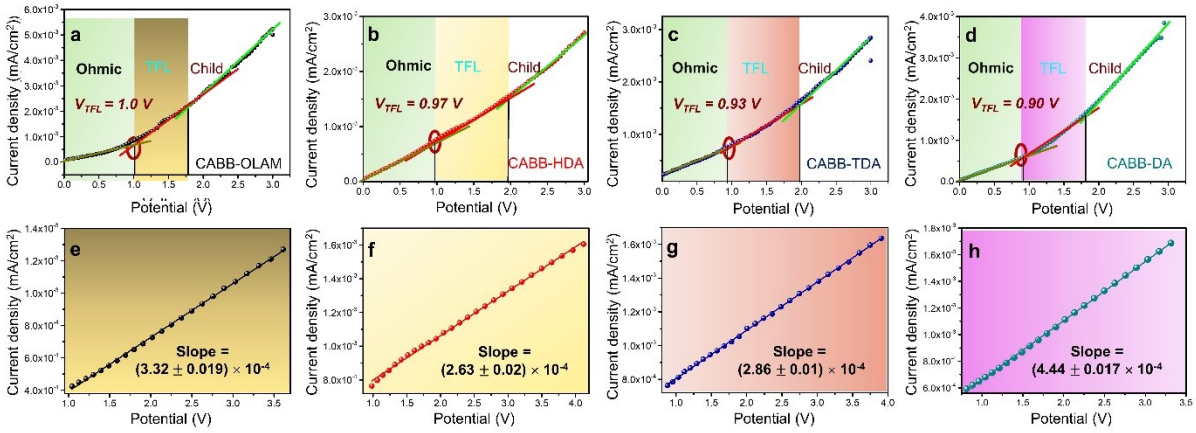

Figure S19. Carrier mobility and trap state density. (a-d) The estimation of V_{TFL} using Mott-Gurney's equation of the electron-only devices under dark for the CABB NCs. (e-h) *J-V* plots for determining the charge carrier mobility (μ) for the CABB NCs.

In the SCLC plots, the first section is the ohmic region where the current increases linearly with potential ($n = 1, J \propto V$), and the second and third sections are the trap-filled limited (TFL) region ($n = 2$) and the child region ($n > 3$).

The trap state density is measured by the first inflection point voltage (V_{TFL}) from the intersection of the first and second regions according to equation (2), where the trap states initially saturate the charge carriers. The second region denotes charge carrier generation and transportation, i.e., $J \propto V^2$. It allows the estimation of electron mobility from the slope of the Mott Gurney's equation (3) by linear fitting of the $J \propto V^2$ plot.

$$\eta = \frac{(2V_{TFL}\varepsilon\varepsilon_0)}{eL^2} \quad \text{(S2)}$$

$$J = \frac{9\mu\varepsilon\varepsilon_0 V^2}{8L^3} \quad \text{(S3)}$$

where η is the trap state density, V_{TFL} is trap-filled limited voltage, ε is the relative dielectric constant value of CABB (ε = 51), ε_o is the vacuum permittivity, L is the thickness of the CABB NC layer, J is the current density (mA/cm^2), and μ is the carrier mobility.

Table S3. Comparative list of the electron mobility of the CABB NCs with the literature reported perovskite NCs, quantum dots, and thin films.

Perovskite	Type	Mobility (cm^2 V^{-1} s^{-1})	References
$Cs_3Cu_2I_5$	Thin film	3.0×10^{-2}	S6
$PEA_2MA_2Pb_3I_{10}$	Thin film	4.4×10^{-2}	S7
$CsPbBr_3$	Quantum dot	1.0×10^{-2}	S8
$MAPbI_3$	Thin film	6.0×10^{-2}	S9
$Cs_2AgBi_{0.6}Sb_{0.4}Br_6$	Nanocrystal	1.9×10^{-3}	S10
$CsPbBr_{1.5}I_{1.5}$	Nanosheet	7.9×10^{-4}	S11
CABB-OLAM	Nanocrystal	$(1.50 \pm 0.08) \times 10^{-2}$	*This work*
CABB-HDA	Nanocrystal	$(1.26 \pm 0.01) \times 10^{-2}$	*This work*
CABB-TDA	Nanocrystal	$(1.30 \pm 0.00) \times 10^{-2}$	*This work*
CABB-DA	Nanocrystal	$(2.00 \pm 0.07) \times 10^{-2}$	*This work*

Table S4. Comparative list of the electron mobility of the CABB NCs with the literature reported lead-free perovskite single crystals.

Perovskite	Type	Mobility (cm^2 V^{-1} s^{-1})	References
$Cs_2AgBiBr_6$	Single crystal	0.49	S12
$Cs_2AgBiBr_6$	Single crystal	0.80	S13
$Cs_3Sb_2I_9$	Single crystal	1.8	S14
$Rb_3Sb_2I_9$	Single crystal	0.32	S14
CABB-OLAM	Nanocrystal	$(1.50 \pm 0.08) \times 10^{-2}$	*This work*
CABB-HDA	Nanocrystal	$(1.26 \pm 0.01) \times 10^{-2}$	*This work*
CABB-TDA	Nanocrystal	$(1.30 \pm 0.00) \times 10^{-2}$	*This work*
CABB-DA	Nanocrystal	$(2.00 \pm 0.07) \times 10^{-2}$	*This work*

Supporting References

S1. S. Adhikari and P. Johari, *Phys. Rev. Mater.* 2023. **7**, 075401.
S2. P. E. Blochl, *Phys. Rev. B: Condens. Matter Mater. Phys.* 1994, **50**, 17953−17979.
S3. P. J. Perdew, K. Burke and M. Ernzerhof, *Phys. Rev. Lett.* 1996, **77**, 3865-3868.
S4. J. Klimes, D. R. Bowler, D and A. Michaelides, *J. Phys.: Condens. Matter.* 2010, **22**, 022201.
S5. R. Tran, Z. Xu, B. Radhakrishnan, D. Winston, W. Sun, K. A. Persson and S. P. Ong, *Sci. Data.* 2016, **3**, 160080.
S6. Z. X. Zhang, C. Li, C, Y. Lu, X. W. Tong, F. X. Liang, X. Y .Zhao, D. Wu, C. Xie and L. B. Luo, *J. Phys. Chem. Lett.* 2019, **10**, 5343–5350.
S7. Y. Zhang, M. Sun, N. Zhou, B. Huang and H. Zhou, *J. Phys. Chem. Lett.* 2020, **11**, 7610–7616.
S8. S. Kumar, and C. J. Shih, *J. Appl. Phys.* 2020, **128**, 120901.
S9. B. Maynard, Q. Long, E. A. Schiff, M. Yang, K. Zhu, R. Kottokkaran, H. Abbas and V. L. Dalal, *Appl. Phys. Lett.* 2016, **108**, 173505.
S10. A. Kumar, S. K. Swami, S. S. Rawat, V. N. Singh, O. P. Sinha and R. Srivastava,. *Int. J. Energy Res.* 2021, **45**, 16769–16780.
S11. A. Mandal, A. Ghosh, D. Ghosh, and S. Bhattacharyya, *ACS Appl. Mater. Interfaces* 2021**, 13**, 43104-43114.
S12. Y. Dang, G. Tong, W. Song, Z. Liu, L. Qiu, L. K. Ono and Y. Qi, *J. Mater. Chem. C* 2019, **8**, 276–284.
S13. Y. Yin, W. Tian, J. Leng, J. Bian and S. Jin, *J. Phys. Chem. Lett.* 2020, **11**, 6956–6963.
S14. K. M. McCall, Z. Liu, G. Trimarchi, C. C. Stoumpos, W. Lin, W, Y. He, I. Hadar, M. G. Kanatzidis and B. W. Wessels, *ACS Photonics* 2018, **5**, 3748–3762.